MATERIALS SCIENCE

New magnetic phase of the chiral skyrmion material Cu_2OSeO_3

Fengjiao Qian[1]*, Lars J. Bannenberg[1], Heribert Wilhelm[2], Grégory Chaboussant[3], Lisa M. Debeer-Schmitt[4], Marcus P. Schmidt[5], Aisha Aqeel[6†], Thomas T. M. Palstra[6‡], Ekkes Brück[1], Anton J. E. Lefering[1], Catherine Pappas[1§], Maxim Mostovoy[6], Andrey O. Leonov[7,8]

The lack of inversion symmetry in the crystal lattice of magnetic materials gives rise to complex noncollinear spin orders through interactions of a relativistic nature, resulting in interesting physical phenomena, such as emergent electromagnetism. Studies of cubic chiral magnets revealed a universal magnetic phase diagram composed of helical spiral, conical spiral, and skyrmion crystal phases. We report a remarkable deviation from this universal behavior. By combining neutron diffraction with magnetization measurements, we observe a new multidomain state in Cu_2OSeO_3. Just below the upper critical field at which the conical spiral state disappears, the spiral wave vector rotates away from the magnetic field direction. This transition gives rise to large magnetic fluctuations. We clarify the physical origin of the new state and discuss its multiferroic properties.

INTRODUCTION

Chiral magnets show a variety of periodically modulated spin states—spirals (*1*, *2*), triangular and square arrays of skyrmion tubes (*3*–*8*), and a cubic lattice of monopoles and antimonopoles (*9*)—which can be viewed as magnetic crystals of different symmetries and dimensionalities. These competing magnetic superstructures show high sensitivity to external perturbations, allowing the control of phase boundaries with applied electric fields and stresses (*10*, *11*). The nontrivial topology of multiply periodic magnetic states gives rise to emergent electromagnetic fields and unconventional spin, charge, and heat transport (*12*–*16*). The stability and small size of magnetic skyrmions as well as low spin currents required to set them into motion paved the way to new prototype memory devices (*17*–*21*).

Recent studies of chiral cubic materials hosting skyrmions, such as the itinerant magnets, MnSi and FeGe, and the Mott insulator, Cu_2OSeO_3, showed that they exhibit the same set of magnetic states with one or more long-period spin modulations and undergo similar transitions under an applied magnetic field (*22*). This universality is a result of noncentrosymmetric cubic lattice symmetry and the hierarchy of energy scales (*2*, *23*, *24*). The transition temperature T_c is determined by the ferromagnetic (FM) exchange interaction J. The relatively weak antisymmetric Dzyaloshinskii-Moriya (DM) interaction, with the strength D proportional to the spin-orbit coupling constant λ, renders the uniform FM state unstable toward a helical spiral modulation (*1*, *25*). It determines the magnitude of the modulation wave vector $\boldsymbol{Q}$ and the value of the critical field H_{C2}, above which the spiral modulation is suppressed. In contrast to low-symmetry systems (*26*, *27*), the DM interaction in cubic chiral magnets does not impose constraints on the direction of the spiral wave vector (*2*). The direction of the wave vector is controlled by the applied magnetic field and magnetic anisotropies of higher order in λ. In the helical spiral phase observed at low magnetic fields, magnetic anisotropies pin the direction of $\boldsymbol{Q}$ either along one of the cubic body diagonals, as in MnSi, or along the cubic axes, as in FeGe or Cu_2OSeO_3. The competition between the Zeeman and magnetic anisotropy energies sets the critical field H_{C1} of the transition between the helical and conical spiral states, above which $\boldsymbol{Q}$ is parallel to the applied magnetic field. In the multiply periodic skyrmion crystal state, the spiral wave vectors are perpendicular to the field direction, which is favored by the nonlinear interaction between the three helical spirals.

Here, we report a remarkable deviation from this well-established universal behavior. By small-angle neutron scattering (SANS) and magnetic measurements, we observe a new low-temperature magnetic phase of Cu_2OSeO_3. At relatively high magnetic fields, $\boldsymbol{Q}$ tilts away from the magnetic field vector, $\boldsymbol{H}$, when this is directed along the [001] crystallographic direction favored by anisotropy at zero field. This transition occurs where it is least expected—at H close to H_{C2} where the dominant Zeeman interaction favors $\boldsymbol{Q} \parallel \boldsymbol{H}$ and at low temperatures where thermal spin fluctuations that can affect the orientation of $\boldsymbol{Q}$ are suppressed. The reorientation of the spiral wave vector is accompanied by strong diffuse scattering, reminiscent of the pressure-induced partially ordered magnetic state in MnSi (*28*). The instability of the conical spiral state at high applied magnetic fields can be considered as a re-entrance into the helical state, although $\boldsymbol{Q}$ in the "tilted conical spiral" state is not close to high-symmetry points. The new phase of Cu_2OSeO_3 is sensitive to the direction of the applied magnetic field: For $\boldsymbol{H} \parallel \langle 110 \rangle$, no tilted spiral state is observed. Instead, we find that the helical-to-conical spiral transition splits into two transitions occurring at slightly different magnetic fields.

We show theoretically that the tilted spiral state originates from the interplay of competing anisotropic spin interactions, which is generic to chiral magnets and may be important for understanding the structure of metastable skyrmion crystal states (*7*, *8*, *29*). This interplay is particularly strong in Cu_2OSeO_3 owing to the composite nature of spin of the magnetic building blocks (*30*). The transition to the new state in multiferroic Cu_2OSeO_3 should have a strong effect on the magnetically induced electric polarization. It should also affect the spin Hall magnetoresistance (*31*) and modify the spin wave spectrum.

[1]Faculty of Applied Sciences, Delft University of Technology, Mekelweg 15, 2629JB Delft, Netherlands. [2]Diamond Light Source Ltd., Chilton, Didcot, Oxfordshire OX11 0DE, UK. [3]Laboratoire Léon Brillouin, CEA-Saclay, 91191 Gif sur Yvette, France. [4]Oak Ridge National Laboratory, Oak Ridge, TN 37831, USA. [5]Max Planck Institute for Chemical Physics of Solids, Nöthnitzer-Straße 40, 01187 Dresden, Germany. [6]Zernike Institute for Advanced Materials, University of Groningen, Nijenborgh 4, 9747 AG Groningen, Netherlands. [7]Department of Chemistry, Hiroshima University, 1-3-1, Kagamiyama, Higashi-Hiroshima 739-8526, Japan. [8]Chiral Research Center, Hiroshima University, 1-3-1, Kagamiyama, Higashi Hiroshima, Hiroshima 739-8526, Japan.
*Present address: Nanjing University of Aeronautics and Astronautics, Nanjing, China.
†Present address: Technical University of Munich, Munich, Germany.
‡Present address: University of Twente, Enschede, Netherlands.
§Corresponding author. Email: c.pappas@tudelft.nl

RESULTS

First hints for the existence of the new phase came from the anomalous field dependence of the magnetization, M, and the ac magnetic susceptibilities, χ' and χ'', shown in section S1. A direct confirmation was provided by SANS, which probes correlations perpendicular to the incoming neutron beam wave vector $\boldsymbol{k}_i$. For this reason, we performed our measurements in two crystallographic orientations and for each orientation in two complementary configurations, $\boldsymbol{H} \perp \boldsymbol{k}_i$ and $\boldsymbol{H} \parallel \boldsymbol{k}_i$, thus providing a full picture of the effect of the magnetic field on the magnetic correlations.

A selection of patterns obtained at $T = 2$ K is shown in Fig. 1 (A and B) for $\boldsymbol{H} \parallel [110]$ and in Fig. 1 (C and D) for $\boldsymbol{H} \parallel [001]$. At zero field, the SANS patterns show four peaks along the diagonal directions in Fig. 1 (A and D) for $\boldsymbol{k}_i \parallel [001]$ and two peaks along the horizontal axis in Fig. 1 (B and C) for $\boldsymbol{k}_i \parallel [110]$. These are the magnetic Bragg peaks of the helical spiral state with wave vectors along the three equivalent ⟨001⟩ crystallographic directions.

At $\mu_0 H = 25$ mT, the scattered intensity vanishes for $\boldsymbol{H} \parallel \boldsymbol{k}_i$ (Fig. 1, B and D) because of the reorientation of the spiral wave vector along the magnetic field at the transition to the conical spiral phase. On the other hand, for $\boldsymbol{H} \perp \boldsymbol{k}_i$ and $\boldsymbol{H} \parallel [110]$, Fig. 1A shows the coexistence of helical spiral and conical spiral peaks (additional weak peaks are attributed to multiple scattering). Thus, the helical-to-conical transition for $\boldsymbol{H} \parallel [110]$ is not a simple one-step process. Reorientation first occurs in the helical spiral domain with the wave vector perpendicular to the field direction $\boldsymbol{Q} \parallel [001]$. It is followed by a gradual reorientation of the wave vectors of the other two helical spiral domains. Upon a further increase of the magnetic field, the conical spiral peaks weaken in intensity and disappear at the transition to the field-polarized collinear spin state, which, for $\boldsymbol{H} \parallel \langle 110 \rangle$, occurs above 75 mT.

The unexpected behavior, a signature of the new phase, is seen in the evolution of SANS patterns for $\boldsymbol{H} \parallel [001]$ in Fig. 1 (C and D). For $\boldsymbol{H} \perp \boldsymbol{k}_i$ (Fig. 1C), the Bragg peaks broaden along the circles with radius Q and eventually split into two well-defined peaks at 35 and 40 mT. This is surprising because, in this configuration, the two peaks along the horizontal axis correspond to the spiral with the wave vector parallel to both the magnetic field and the cubic axis. Thus, no reorientation is expected for the spiral domain favored by both the Zeeman interaction and magnetic anisotropy. In addition to the splitting of the Bragg peaks, in the complementary configuration of $\boldsymbol{H} \parallel \boldsymbol{k}_i$ shown in Fig. 1D, a broad ring of scattering develops well inside the circle with radius Q.

With increasing temperature, the splitting of the Bragg peaks becomes smaller and disappears at ~50 K, as shown in Fig. 2A. At $T = 10$ K, the scattered intensity on the circle with radius Q, when plotted against the azimuthal angle ϕ, consists of two Gaussians peaks, labeled 1 and 2 (Fig. 2B). These are centered at two distinct angles, which vary with temperature, and their difference reaches 30° at $T = 2$ K (Fig. 2C). The integrated intensities depicted in Fig. 2D show that peak 2, which splits away from the conical spiral peak 1, is by far the more intense one. Its intensity goes through a maximum at ~35 K and then decreases at low temperatures, possibly because the optimum Bragg condition is not fulfilled any longer as the peak moves away from the magnetic field direction.

Our experimental findings are summarized in Fig. 3, which shows contour plots of the real and imaginary susceptibilities, χ' and χ'', as well as the phase boundaries obtained by SANS. Close to T_c, the

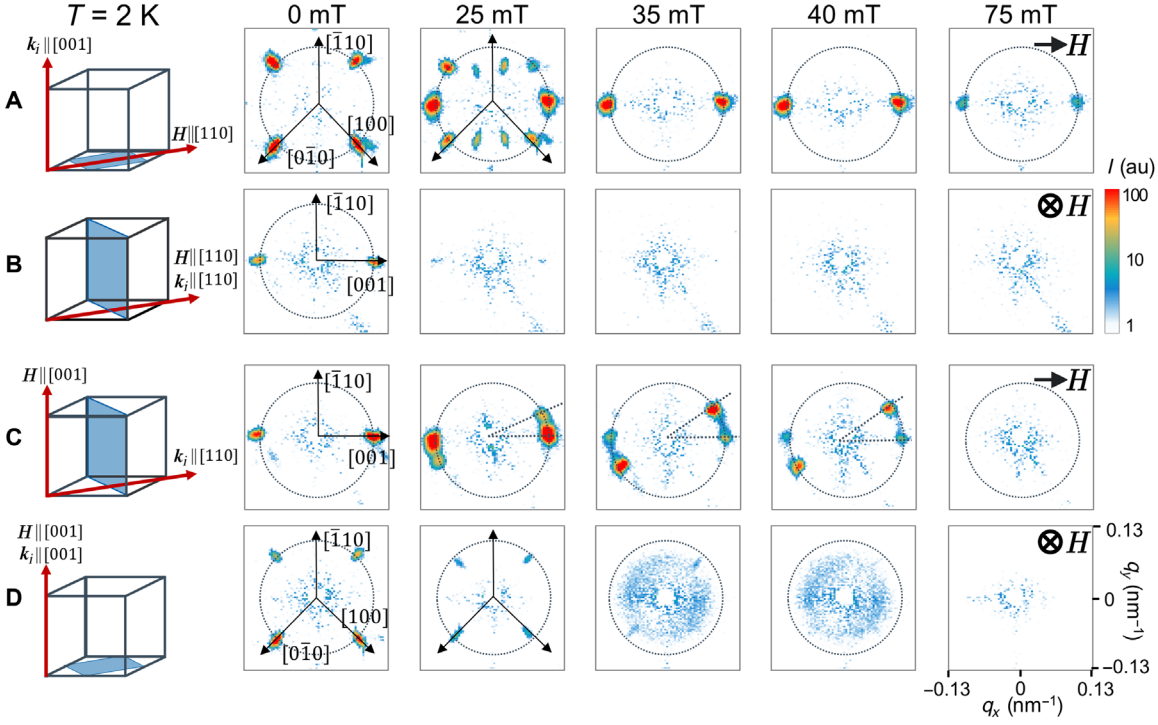

Fig. 1. Magnetic field dependence of the Cu_2OSeO_3 SANS patterns at $T = 2$ K. The first column illustrates the geometry of the experiment: $\boldsymbol{H} \parallel [110]$ in (**A**) and (**B**) and $\boldsymbol{H} \parallel [001]$ in (**C**) and (**D**). The orientation of the neutron beam wave vector is $\boldsymbol{k}_i \perp \boldsymbol{H}$ in (A) and (C) and $\boldsymbol{k}_i \parallel \boldsymbol{H}$ in (B) and (D). The blue planes illustrate the SANS detection plane. The radius of the dashed circles on the SANS patterns corresponds to the modulus of the helical spiral propagation vector $Q = 2\pi/\ell \sim 0.1$ nm^{-1}, with $\ell \sim 60$ nm being the pitch of the helix. au, arbitrary units.

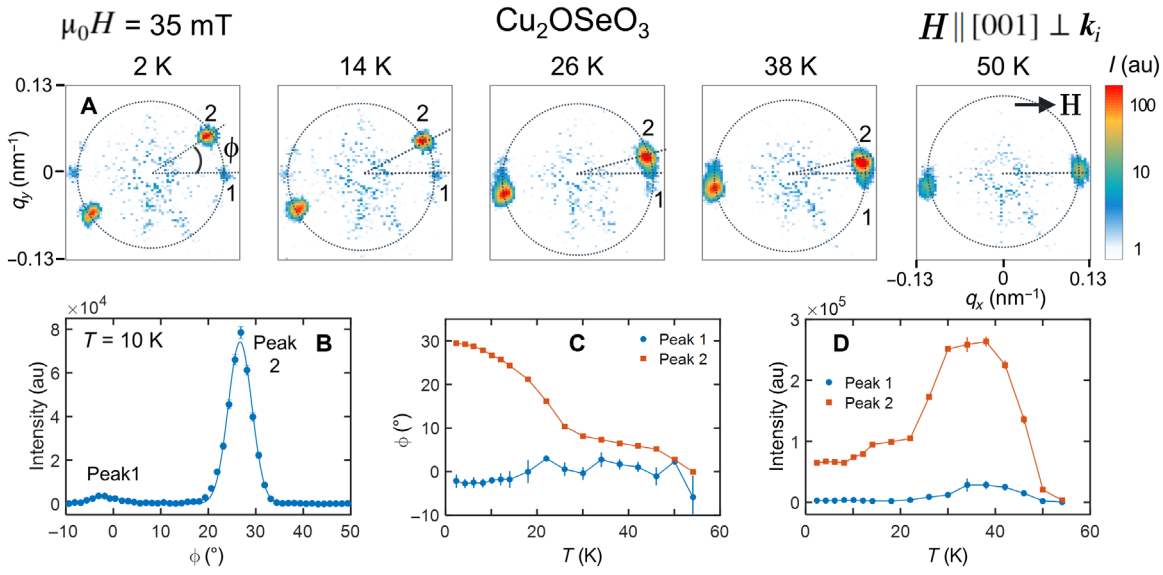

Fig. 2. Temperature dependence of the tilt. (**A**) Temperature dependence of the SANS patterns and (**B** to **D**) the corresponding data analysis. The dashed circles on the SANS patterns are a guide to the eye and have a radius of $Q = 2\pi/\ell \sim 0.1$ nm^{-1}. The angular dependence of the scattered intensity along the circle with radius Q is given in (B) for T = 10 K. The solid lines indicate a fit with two Gaussian peaks labeled 1 and 2 in the SANS patterns. The temperature dependence of the angular positions and integrated intensities of the two peaks is shown in (C) and (D), respectively.

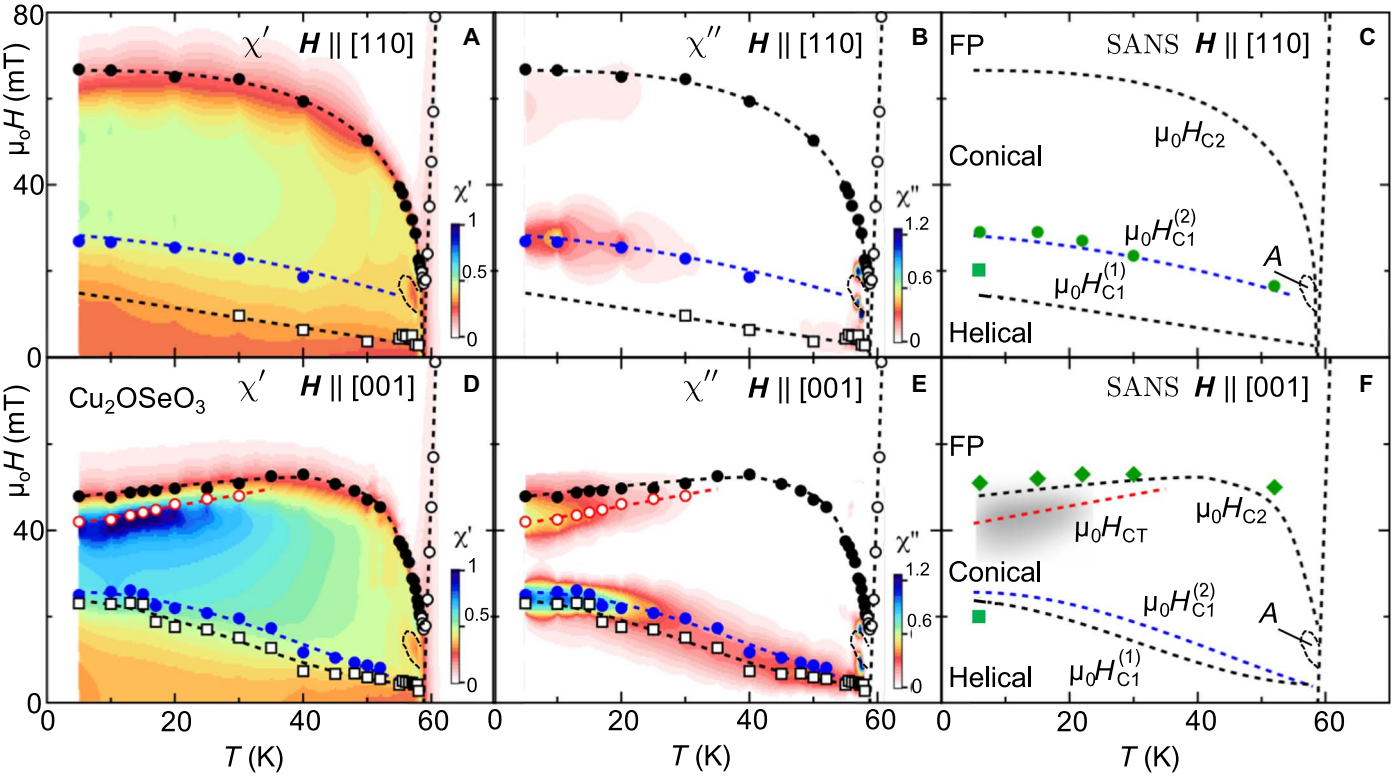

Fig. 3. Phase diagrams from ac magnetic susceptibilities. Contour plots of χ' and χ'' at a frequency of 10 Hz and phase boundaries obtained by SANS for $\boldsymbol{H} \parallel [110]$ (**A** to **C**) and $\boldsymbol{H} \parallel [001]$ (**D** to **F**). The units for χ' and χ'' are 10^{-4} and 10^{-6} m^3/mol$_{Cu}$, respectively. The helical, conical, *A*, tilted spiral (TS), and field-polarized (FP) phases are indicated in (C) and (F). The phase boundaries determined from the susceptibility are illustrated by the symbols and the dashed lines in (A), (B), (D), and (E). They correspond to the peaks of χ'', with the exception of $\mu_0 H_{C2}$, which is defined by the inflection point of χ' versus $\mu_0 H$. These criteria are the same as in our previous study (*39*). At low fields, two lines $\mu_0 H_{C1}^{(1)}$ and $\mu_0 H_{C1}^{(2)}$ are identified below 50 K. Just below $\mu_0 H_{C2}$, a red dashed line denoted as $\mu_0 H_{CT}$ in (D) to (F) marks the onset of the "tilted spiral" state for $\boldsymbol{H} \parallel \langle 001 \rangle$. The phase boundaries determined from SANS are illustrated by the green symbols in (C) and (F). The shaded gray area just below $\mu_0 H_{C2}$ in (F) marks the region where the ring of scattering emerges for $\boldsymbol{H} \parallel [001] \parallel \boldsymbol{k}_i$.

transition from the helical to the conical phase is marked by a single $\mu_0 H_{C1}(T)$ line, which, at low temperatures, evolves into two lines, $\mu_0 H_{C1}^{(1)}(T)$ and $\mu_0 H_{C1}^{(2)}(T)$, derived from the two adjacent χ'' peaks (see fig. S1, C and F, and the discussion in the Supplementary Materials). The most prominent difference between the two field orientations appears close to $\mu_0 H_{C2}$ below 30 K. In this field and temperature range, clear maxima are seen in both χ' and χ'' for $\boldsymbol{H} \parallel [001]$. These define a new line $\mu_0 H_{CT}(T)$ (red dashed line in Fig. 3, D to F), which shifts slightly to lower magnetic fields with decreasing temperature.

The boundaries determined from the SANS measurements, shown in Fig. 3 (C and F), are in excellent agreement with those derived from susceptibility. Furthermore, it is remarkable that the shaded area in Fig. 3F, which marks the region where the ring of scattering shown in Fig. 1D emerges for $\boldsymbol{H} \parallel \langle 001 \rangle \parallel \boldsymbol{k}_i$, coincides with the maxima of χ' and χ''.

DISCUSSION

This remarkable behavior can be understood in terms of competing magnetic anisotropies that are generic to cubic chiral magnets. This competition is particularly tight in Cu_2OSeO_3, as explained below. Despite the long history of studies of cubic chiral magnets (*2*, *23*, *24*), the discussion of anisotropic magnetic interactions in these materials remains, to the best of our knowledge, incomplete.

The starting point of our approach is a continuum model with the free energy per unit cell

$$\varepsilon = \frac{Ja^2}{2} \sum_{i=x,y,z} \partial_i \boldsymbol{m} \cdot \partial_i \boldsymbol{m} + Da\ \boldsymbol{m} \cdot \nabla \times \boldsymbol{m} - a^3 \mu_0 M \boldsymbol{m} \cdot \boldsymbol{H} + \varepsilon_a \quad (1)$$

where $\boldsymbol{m}$ is the unit vector in the direction of the magnetization, M is the magnetization value, a is the lattice constant, and ε_a is the magnetic anisotropy energy. There are five terms of fourth order in the spin-orbit coupling, λ, allowed by the $P2_13$ symmetry

$$\begin{aligned}
\varepsilon_a \;=\; & C_1 a^2 \left[\partial_x m_x \partial_x m_x + \partial_y m_y \partial_y m_y + \partial_z m_z \partial_z m_z\right] \\
& + C_2 a^2 \left[\partial_z m_x \partial_z m_x + \partial_x m_y \partial_x m_y + \partial_y m_z \partial_y m_z \right. \\
& \left. - (\partial_y m_x \partial_y m_x + \partial_z m_y \partial_z m_y + \partial_x m_z \partial_x m_z)\right] \\
& + 2C_3 a^2 \left[\partial_x m_x \partial_y m_y + \partial_y m_y \partial_z m_z + \partial_z m_z \partial_x m_x\right] \\
& + \frac{1}{2} \mathcal{J} a^4 \left[\partial_x^2 \boldsymbol{m} \cdot \partial_x^2 \boldsymbol{m} + \partial_y^2 \boldsymbol{m} \cdot \partial_y^2 \boldsymbol{m} + \partial_z^2 \boldsymbol{m} \cdot \partial_z^2 \boldsymbol{m}\right] \\
& + K\left(m_x^4 + m_y^4 + m_z^4\right) \qquad (2)
\end{aligned}$$

Their importance can be understood by substituting into Eq. 1 the conical spiral Ansatz

$$\boldsymbol{m} = \cos\theta \boldsymbol{e}_3 + \sin\theta [\cos(\boldsymbol{Q} \cdot \boldsymbol{x}) \boldsymbol{e}_1 + \sin(\boldsymbol{Q} \cdot \boldsymbol{x}) \boldsymbol{e}_2] \quad (3)$$

where θ is the conical angle and $(\boldsymbol{e}_1, \boldsymbol{e}_2, \boldsymbol{e}_3)$ are three mutually orthogonal unit vectors. If the magnetic anisotropy and Zeeman energies are neglected, $Qa = \frac{D}{J}$ is independent of the orientation of $\boldsymbol{Q}$. The applied magnetic field favors $\boldsymbol{Q} \parallel \boldsymbol{H}$ with the conical angle given by $\cos\theta = \frac{H}{H_{C2}}$, where $\mu_0 M H_{C2} = \frac{D^2}{Ja^3}$ defines the critical field H_{C2}.

The DM interaction originates from the antisymmetric anisotropic exchange between Cu spins, which is the first-order correction to the Heisenberg exchange in powers of λ: $D \sim J\zeta$, where $\zeta = \frac{\lambda}{\Delta}$, Δ being the typical electron excitation energy on Cu sites (*25*, *32*). The first three anisotropy terms in Eq. 2 result from the symmetric anisotropic exchange between Cu ions and are proportional to the second power of the spin-orbit coupling (*25*, *32*): $C_i \sim J\zeta^2$. Since $Qa = \frac{D}{J} = \zeta$, these anisotropy terms are of the order of $J\zeta^4$. The fourth term in Eq. 2 results from the expansion of the Heisenberg exchange interaction in powers of Qa and is also $\sim J\zeta^4$. The last term in Eq. 2 has the form of the fourth-order single-ion anisotropy allowed by cubic symmetry. In absence of the single-ion anisotropy for Cu ions with $S = \frac{1}{2}$, this term emerges at the scale of the unit cell containing 16 Cu ions, which form a network of tetrahedra with $S = 1$ (*30*, *33*). This last term appears either as a second-order correction to the magnetic energy in powers of the symmetric anisotropic exchange or as a fourth-order correction in the antisymmetric exchange, both $\propto \zeta^4$. The intermediate states are excited states of Cu tetrahedra (*34*) with energy $\sim J$ rather than the electronic excitations of Cu ions with energy Δ. As a result, the last term is also $\sim J\zeta^4$. Therefore, the magnetic block structure of Cu_2OSeO_3 makes all anisotropy terms in Eq. 2 comparable, which can frustrate the direction of $\boldsymbol{Q}$. We note that the ferrimagnetic nature of Cu_2OSeO_3 does not play an important role: For the magnetic fields considered here and the large spin gap in the spin tetrahedron of about 275 K (*30*), the tilt angle between the two magnetic sublattices should be less than 10^{-4} and can be neglected.

Another important point is that the direction of $\boldsymbol{Q}$, favored by a magnetic anisotropy term, may vary with the strength of the applied magnetic field because it depends on the conical angle, $\theta = \theta(H)$. Figure S6 shows the θ dependence of the fourth-order effective anisotropy, $K_{eff} = KB(\theta)$, which is negative for small θ and for $\theta \sim \frac{\pi}{2}$, stabilizing the helical spiral with $\boldsymbol{Q} \parallel \langle 001 \rangle$, as it is the case for Cu_2OSeO_3 at zero field. However, for intermediate values of θ, K_{eff} is positive and the preferred direction of $\boldsymbol{Q}$ becomes $\langle 111 \rangle$. In this interval of θ, spins in the conical spiral with $\boldsymbol{Q} \parallel \langle 001 \rangle$ are closer to the body diagonals than to cubic axes, which makes this wave vector direction unfavorable (see section S4 for more details).

This effect gives rise to local minima of the conical spiral energy in Q-space. If only the fourth-order anisotropy is taken into account, the global energy minimum for $\boldsymbol{H} \parallel \langle 001 \rangle$ is still at $\boldsymbol{Q} \parallel \boldsymbol{H}$. However, additional anisotropy terms can turn these local minima into global ones, such that, in some magnetic field intervals, the tilted conical spiral becomes the ground state. Figure 4 (A to F) shows the false color plot of the conical spiral energy as a function of $\boldsymbol{Q}$ for several values of the dimensionless magnetic field, $h = H/H_{C2}$, applied along the [001] direction. For simplicity, only two anisotropy terms are nonzero in this calculation: $\kappa = \frac{KJ}{D^2} = -0.19$ and $\gamma_1 = \frac{C_1}{J} = -0.1$. In zero field (Fig. 4A), there are three energy minima along $\langle 001 \rangle$, that is, along the [001], [010], and [001] directions, corresponding to three degenerate helical spiral domains in Cu_2OSeO_3. For $h = 0.2$ (Fig. 4B), the helical spiral states with $\boldsymbol{Q}$ along the [001] and [010] directions are metastable. For $h = 0.3$ (Fig. 4C), only the minimum with $\boldsymbol{Q} \parallel [001]$ exists, corresponding to the conical spiral state. For $h = 0.6$ (Fig. 4D), the conical spiral with $\boldsymbol{Q} \parallel [001]$ is unstable and there appear four new minima, corresponding to four domains with $\boldsymbol{Q}$ tilted away from the magnetic field vector along the $[\pm 1, \pm 1, 0]$ directions, as can be seen more clearly in Fig. 4F showing the energy sphere seen from above. The relative energy changes in this

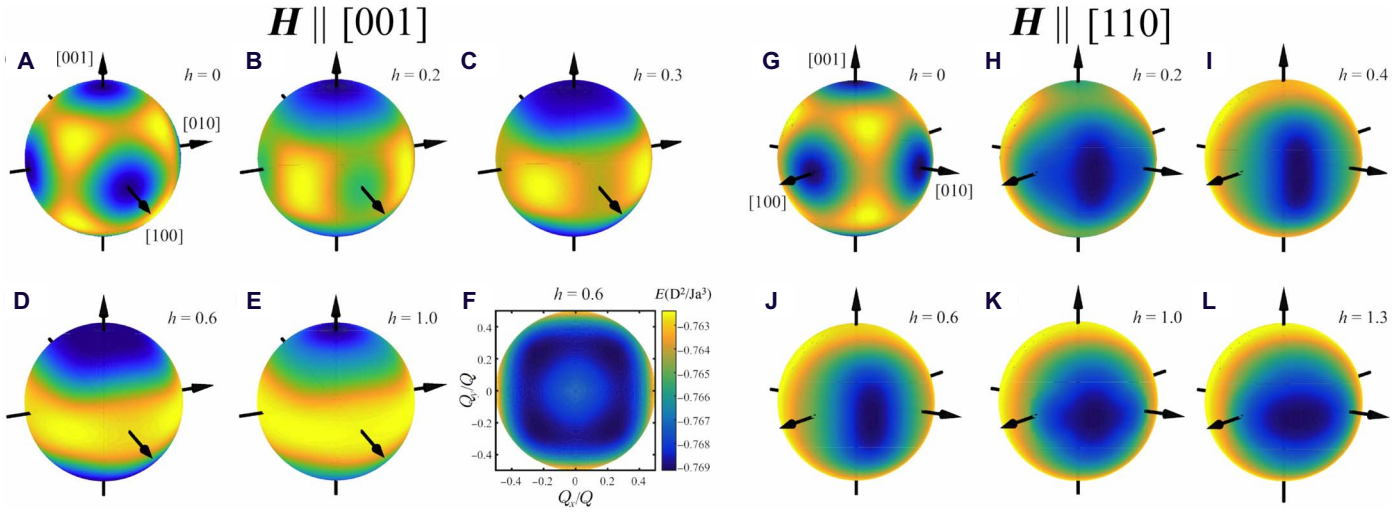

Fig. 4. *Q* dependence of spiral energy for *H* ∥ [001] and *H* ∥ [110]. False color plots of the conical spiral energy on the unit sphere of $\hat{\boldsymbol{Q}} = \boldsymbol{Q}/Q$ describing the direction of the spiral wave vector for various values of the dimensionless magnetic field, $h = H/H_{C2}$. (**A** to **F**) Magnetic field applied along the [001] direction: (A) $h = 0$, (B) $h = 0.2$, (C) $h = 0.3$, (D) $h = 0.6$, and (E) $h = 1.0$. (F) The energy sphere for $h = 0.6$, seen from above, showing four energy minima, which correspond to ***Q*** tilted away from the magnetic field vector along the [±1, ±1, 0] directions. (**G** to **L**) Magnetic field applied along the [110] direction: (G) $h = 0$, (H) $h = 0.2$, (I) $h = 0.4$, (J) $h = 0.6$, (K) $h = 1.0$, and (L) $h = 1.3$.

part are ~ 10^{-2}, implying large fluctuations of the spiral wave vector, which can explain the diffuse scattering shown in Fig. 1D. Finally, Fig. 4E shows the field-polarized state at $h = 1$.

Figure 4 (G to L) shows the ***Q*** dependence of the conical spiral energy in several magnetic fields along the [110] direction, calculated for the same values of parameters as those in Fig. 4 (A to F). As the magnetic field increases, the helical spiral states with ***Q*** along the [001] and [010] directions merge into a single state with the wave vector parallel to ***H***, and the state with ***Q*** ∥ [001] ultimately disappears (see Fig. 4, G to I). This gives rise to the two-step transition from the helical to the conical phase observed experimentally. For this field direction, the multidomain tilted spiral state does not appear and there is only one global minimum with ***Q*** ∥ ***H*** ∥ [110] for $H > H_{C1}$. Nevertheless, one can see the strong vertical elongation of the energy contours in Fig. 4 (H to J), which is a result of the competition with the ***Q*** ∥ [11 ±1] states. At $h = 1$, the elongation changes from vertical to horizontal (see Fig. 4, K and L).

These conclusions drawn using the variational approach are confirmed by exact energy minimization of Eq. 1 including two competing anisotropy terms: the fourth-order anisotropy with $\kappa = -0.2$ and the anisotropic exchange γ_1. The case of ***H*** ∥ [110] is treated in section S5, which explains the two lines $\mu_0 H_{C1}^{(1)}$ and $\mu_0 H_{C1}^{(2)}$, for the transition from the helical to the conical spiral state, shown in Fig. 3 (A to C). For ***H*** ∥ [001], the field dependence of the angle, ϕ, between ***Q*** and the [001] cubic axis, which describes the tilt of ***Q*** toward the ⟨111⟩ directions, is shown in Fig. 5A. The tilted spiral state appears when $|\gamma_1|$ exceeds a critical value, which is slightly lower than 0.1 for $\kappa = -0.2$. When the magnetic field increases, the tilt angle reaches its maximal value, ϕ_{max}, marked by the empty circles in Fig. 5A, and then decreases to 0. As shown in Fig. 5B, $\phi_{max} = 0$ for $|\gamma_1| \lesssim 0.1$. Thus, the state with ***Q*** ∥ ⟨100⟩ is stable at low anisotropies. However, as the exchange anisotropy increases, an intermediate state occurs, and finally, for $|\gamma_1| \gtrsim 0.28$, the state with ***Q*** ∥ ⟨111⟩ is stabilized even at zero magnetic field.

In our diffraction experiment, we do not observe all four tilted spiral domains, which is likely related to a small misalignment of the sample: Because of a weak dependence of the spiral energy on ***Q***, even a tiny

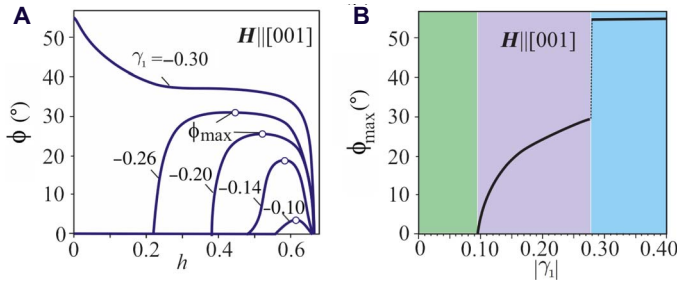

Fig. 5. Field-induced reorientation of the spiral wave vectors for the fourth-order anisotropy $\kappa = -0.2$ and the anisotropic exchange $\gamma_1 < 0$. (**A**) Magnetic field dependence of the angle ϕ describing the tilt of the spiral wave vector ***Q*** away from ***H*** ∥ [001] toward the body diagonals for different values of $|\gamma_1|$. Above the critical value, $|\gamma_1| \approx 0.1$, ϕ increases from 0, which corresponds to the conical spiral phase, to a maximal value, ϕ_{max} (empty circle), and then decreases back to 0 as the magnetic field strength, *h*, increases. For $|\gamma_1| \gtrsim 0.28$, ***Q*** ∥ ⟨111⟩ even at zero field and smoothly rotates toward [001] with increasing field. (**B**) Dependence of ϕ_{max}. For $|\gamma_1| \lesssim 0.1$ (green area), $\phi_{max} = 0$, which implies that ***Q*** ∥ ⟨100⟩. By increasing the strength of the anisotropic exchange, ***Q*** smoothly rotates toward ⟨111⟩ (purple area), and for $|\gamma_1| \gtrsim 0.28$, ***Q*** ∥ ⟨111⟩ (blue area).

deviation of ***H*** from the [001] direction leads to the selection of one of the four domains. This suggests that the domain structure of the tilted state can also be controlled by an applied electric field using the multiferroic nature of Cu_2OSeO_3 (*35*–*37*). The electric polarization induced by the tilted spiral with the spin rotation axis $\boldsymbol{l} = (\frac{1}{\sqrt{2}}\sin\alpha, \frac{1}{\sqrt{2}}\sin\alpha, \cos\alpha)$ is given by

$$\langle \boldsymbol{P} \rangle = \lambda \frac{(3\cos^2\theta - 1)}{4\sqrt{2}} \left(\sin 2\alpha, \sin 2\alpha, \frac{1}{\sqrt{2}}(1 - \cos 2\alpha) \right) \quad (4)$$

For small anisotropies, α is close to the tilt angle of ***Q***, ϕ (a more precise relation between α and ϕ and the derivation of Eq. 4 can be

found in section S6). Since ϕ does not exceed 30°, the induced electric polarization is almost normal to the applied magnetic field $\boldsymbol{H} \parallel [001]$. The conical spiral with $\alpha = 0$ induces no electric polarization.

To summarize, we found a new high-field multidomain magnetic state that intervenes between the conical spiral and field-polarized phases and is stable in a broad temperature range. This major deviation from universal behavior has important consequences for the field of chiral magnetism, for example, the partial magnetic order observed in MnSi under pressure (*28*), electric polarization induced through the magneto-electric coupling, spin Hall magnetoresistance, and anomalies in the spin wave spectrum. The spiral tilt can also give rise to new topological magnetic defects, such as skyrmions, with interesting static and dynamic properties. Our theoretical model that takes into account all competing magnetic anisotropies is in a semiquantitative agreement with experiment. For particular directions of the magnetic field, this competition may stabilize skyrmions (*38*) or new tilted phases. Although the spiral wave vector tilts toward the ⟨111⟩ directions, the energy difference with $\boldsymbol{Q}$ along the ⟨100⟩ directions is relatively small. Therefore, one may envisage the formation of a superstructure with smooth rotation from one spiral domain to another, that is, a conical spiral composed of tilted spirals.

MATERIALS AND METHODS

Magnetization and magnetic susceptibility measurements were performed on two single crystals of Cu_2OSeO_3 with dimensions of ~1 mm × 1 mm × 1 mm grown at the Zernike Institute for Advanced Materials. One crystal was oriented with a ⟨001⟩ axis vertical, while the other one was oriented with a ⟨110⟩ axis vertical. A third single crystal with dimensions of ~3 mm × 3 mm × 4 mm grown at the Max Planck Institute for Chemical Physics of Solids was used for the neutron scattering measurements. This sample was oriented with the $[\bar{1}10]$ crystallographic axis vertical. All crystals were prepared by chemical vapor transport method, and their quality and structure were checked by x-ray diffraction.

Magnetization and magnetic susceptibility were measured with an MPMS 5XL SQUID using the extraction method. For the determination of the magnetization, a static magnetic field, $\mu_0 H$, was applied along the vertical direction. The real and imaginary parts of the magnetic ac susceptibility, χ' and χ'', were measured by adding to $\mu_0 H$ a vertical drive ac field, $\mu_0 H_{ac}$, with an amplitude of 0.4 mT. The frequency of H_{ac} was varied between 0.1 and 1000 Hz.

The SANS measurements were performed on the instruments PA20 of the Laboratoire Léon Brillouin and GP-SANS of the Oak Ridge National Laboratory using neutron wavelengths of 0.6 and 1 nm, respectively. At both instruments, the magnetic field was applied either parallel or perpendicular to the incoming neutron beam wave vector $\boldsymbol{k}_i$ using a horizontal magnetic field cryomagnet. The orientation of the crystal axes with respect to $\boldsymbol{k}_i$ and to the magnetic field was varied by rotating the sample in the cryomagnet. The SANS patterns were collected for $\boldsymbol{H} \parallel [110]$ and $\boldsymbol{H} \parallel [001]$ and, in each case, for $\boldsymbol{H} \perp \boldsymbol{k}_i$ and $\boldsymbol{H} \parallel \boldsymbol{k}_i$, by rotating both the sample and the magnetic field through 90° with respect to $\boldsymbol{k}_i$. Measurements at 70 K, where the magnetic scattering is negligible, were used for the background correction of the SANS patterns.

All measurements were performed after zero field cooling the sample through the magnetic transition temperature, T_c, down to the temperature of interest. The magnetic field was then increased stepwise. The applied magnetic field, $\mu_0 \boldsymbol{H}_{ext}$, was corrected for the demagnetizing effect to obtain the internal magnetic field, $\mu_0 \boldsymbol{H}_{int}$ (in SI units)

$$\boldsymbol{H}_{int} = \boldsymbol{H}_{ext} - N\boldsymbol{M} \tag{5}$$

where $N = {}^1/_3$ is the demagnetization factor for our (nearly) cubic shape samples The demagnetizing field correction also modifies the values of the magnetic susceptibility

$$\chi_{int} = \frac{\chi_{ext}}{1 - \mu_0 N \chi_{ext}} \tag{6}$$

SUPPLEMENTARY MATERIALS

Supplementary material for this article is available at http://advances.sciencemag.org/cgi/content/full/4/9/eaat7323/DC1

Section S1. Temperature and magnetic field dependence of the magnetization and susceptibility
Section S2. Frequency dependence of the ac susceptibility
Section S3. Phase boundaries determined from SANS
Section S4. Effect of magnetic anisotropy on the direction of the spiral wave vector
Section S5. Numerical studies of spiral reorientation processes in the presence of competing anisotropies
Section S6. Electric polarization
Fig. S1. Magnetic properties of Cu_2OSeO_3.
Fig. S2. Temperature dependence of the magnetization.
Fig. S3. χ' and χ'' as a function of magnetic field.
Fig. S4. Frequency dependence of χ' and χ'' at $T = 5$ K.
Fig. S5. Magnetic field dependence of the SANS intensity at 6 K.
Fig. S6. Effective anisotropy.
Fig. S7. Spiral reorientation for $\boldsymbol{H} \parallel [001]$.
Fig. S8. Spiral reorientation for $\boldsymbol{H} \parallel [110]$.
Fig. S9. Field-induced reorientation of the spiral wave vectors for $\boldsymbol{H} \parallel [001]$ and for the fourth-order anisotropy $\kappa = -0.2$ and the anisotropic exchange $\gamma_1 < 0$.
Reference (*40*)

REFERENCES AND NOTES

1. I. E. Dzyaloshinskii, Theory of helicoidal structures in antiferromagnets. I. Nonmetals. *Sov. Phys. JETP* **19**, 960 (1964).
2. P. Bak, M. H. Jensen, Theory of helical magnetic structures and phase transitions in MnSi and FeGe. *J. Phys. C Solid State Phys.* **13**, L881 (1980).
3. A. Bogdanov, A. Hubert, The stability of vortex-like structures in uniaxial ferromagnets. *J. Magn. Magn. Mater.* **195**, 182–192 (1999).
4. S. Mühlbauer, B. Binz, F. Jonietz, C. Pfleiderer, A. Rosch, A. Neubauer, R. Georgii, P. Böni, Skyrmion lattice in a chiral magnet. *Science* **323**, 915–919 (2009).
5. X. Z. Yu, Y. Onose, N. Kanazawa, J. H. Park, J. H. Han, Y. Matsui, N. Nagaosa, Y. Tokura, Real-space observation of a two-dimensional skyrmion crystal. *Nature* **465**, 901–904 (2010).
6. A. K. Nayak, V. Kumar, T. Ma, P. Werner, E. Pippel, R. Sahoo, F. Damay, U. K. Rößler, C. Felser, S. S. P. Parkin, Magnetic antiskyrmions above room temperature in tetragonal Heusler materials. *Nature* **548**, 561–566 (2017).
7. K. Karube, J. S. White, N. Reynolds, J. L. Gavilano, H. Oike, A. Kikkawa, F. Kagawa, Y. Tokunaga, H. M. Rønnow, Y. Tokura, Y. Taguchi, Robust metastable skyrmions and their triangular–square lattice structural transition in a high-temperature chiral magnet. *Nat. Mater.* **15**, 1237–1242 (2016).
8. T. Nakajima,H. Oike, A. Kikkawa, E. P. Gilbert, N. Booth, K. Kakurai, Y. Taguchi, Y. Tokura, F. Kagawa, T.-H. Arima, Skyrmion lattice structural transition in MnSi. *Sci. Adv.* **3**, e1602562 (2017).
9. N. Kanazawa, Y. Nii, X.-X. Zhang, A. S. Mishchenko, G. De Filippis, F. Kagawa, Y. Iwasa, N. Nagaosa, Y. Tokura, Critical phenomena of emergent magnetic monopoles in a chiral magnet. *Nat. Commun.* **7**, 11622 (2016).
10. Y. Okamura, F. Kagawa, S. Seki, Y. Tokura, Transition to and from the skyrmion lattice phase by electric fields in a magnetoelectric compound. *Nat. Commun.* **7**, 12669 (2016).
11. Y. Nii, T. Nakajima, A. Kikkawa, Y. Yamasaki, K. Ohishi, J. Suzuki, Y. Taguchi, T. Arima, Y. Tokura, Y. Iwasa, Uniaxial stress control of skyrmion phase. *Nat. Commun.* **6**, 8539 (2015).
12. M. Lee, W. Kang, Y. Onose, Y. Tokura, N. P. Ong, Unusual Hall effect anomaly in MnSi under pressure. *Phys. Rev. Lett.* **102**, 186601 (2009).

13. A. Neubauer, C. Pfleiderer, B. Binz, A. Rosch, R. Ritz, P. G. Niklowitz, P. Böni, Topological Hall effect in the *A* phase of MnSi. *Phys. Rev. Lett.* **102**, 186602 (2009).
14. J. Zang, M. Mostovoy, J. H. Han, N. Nagaosa, Dynamics of Skyrmion crystals in metallic thin films. *Phys. Rev. Lett.* **107**, 136804 (2011).
15. T. Schulz, R. Ritz, A. Bauer, M. Halder, M. Wagner, C. Franz, C. Pfleiderer, K. Everschor, M. Garst, A. Rosch, Emergent electrodynamics of skyrmions in a chiral magnet. *Nat. Phys.* **8**, 301–304 (2012).
16. N. Nagaosa, Y. Tokura, Topological properties and dynamics of magnetic skyrmions. *Nat. Nanotechnol.* **8**, 899–911 (2013).
17. A. Fert, V. Cros, J. Sampaio, Skyrmions on the track. *Nat. Nanotechnol.* **8**, 152–156 (2013).
18. W. Jiang, P. Upadhyaya, W. Zhang, G. Yu, M. B. Jungfleisch, F. Y. Fradin, J. E. Pearson, Y. Tserkovnyak, K. L. Wang, O. Heinonen, S. G. E. te Velthuis, A. Hoffmann, Blowing magnetic skyrmion bubbles. *Science* **349**, 283–286 (2015).
19. C. Moreau-Luchaire, C. Moutafis, N. Reyren, J. Sampaio, C. A. F. Vaz, N. Van Horne, K. Bouzehouane, K. Garcia, C. Deranlot, P. Warnicke, P. Wohlhüter, J.-M. George, M. Weigand, J. Raabe, V. Cros, A. Fert, Additive interfacial chiral interaction in multilayers for stabilization of small individual skyrmions at room temperature. *Nat. Nanotechnol.* **11**, 444–448 (2016).
20. S. Woo, K. Litzius, B. Krüger, M.-Y. Im, L. Caretta, K. Richter, M. Mann, A. Krone, R. M. Reeve, M. Weigand, P. Agrawal, I. Lemesh, M.-A. Mawass, P. Fischer, M. Kläui, G. S. D. Beach, Observation of room-temperature magnetic skyrmions and their current-driven dynamics in ultrathin metallic ferromagnets. *Nat. Mater.* **15**, 501–506 (2016).
21. A. Fert, N. Reyren, V. Cros, Magnetic skyrmions: Advances in physics and potential applications. *Nat. Mater.* **2**, 17031 (2017).
22. A. Bauer, C. Pfleiderer, *Topological Structures in Ferroic Materials* (Springer International Publishing, 2016), pp. 1–28.
23. O. Nakanishi, A. Yanase, A. Hasegawa, M. Kataoka, The origin of the helical spin density wave in MnSi. *Solid State Commun.* **35**, 995–998 (1980).
24. D. Belitz, T. R. Kirkpatrick, A. Rosch, Theory of helimagnons in itinerant quantum system. *Phys. Rev. B* **73**, 54431 (2006).
25. T. Moriya, Anisotropic superexchange interaction and weak ferromagnetism. *Phys. Rev.* **120**, 91–98 (1960).
26. Y. Togawa, T. Koyama, K. Takayanagi, S. Mori, Y. Kousaka, J. Akimitsu, S. Nishihara, K. Inoue, A. S. Ovchinnikov, J. Kishine, Chiral magnetic soliton lattice on a chiral helimagnet. *Phys. Rev. Lett.* **108**, 107202 (2012).
27. I. Kézsmárki, S. Bordács, P. Milde, E. Neuber, L. M. Eng, J. S. White, H. M. Rønnow, C. D. Dewhurst, M. Mochizuki, K. Yanai, H. Nakamura, D. Ehlers, V. Tsurkan, A. Loidl, Néel-type skyrmion lattice with confined orientation in the polar magnetic semiconductor GaV_4S_8. *Nat. Mater.* **14**, 1116–1122 (2015).
28. C. Pfleiderer, D. Reznik, L. Pintschovius, H. Löhneysen, M. Garst, A. Rosch, Partial order in the non-Fermi-liquid phase of MnSi. *Nature* **427**, 227–231 (2004).
29. L. J. Bannenberg, K. Kakurai, F. Qian, E. Lelièvre-Berna, C. D. Dewhurst, Y. Onose, Y. Endoh, Y. Tokura, C. Pappas, Extended skyrmion lattice scattering and long-time memory in the chiral magnet $Fe_{1-x}Co_xSi$. *Phys. Rev. B* **94**, 104406 (2016).
30. O. Janson, I. Rousochatzakis, A. A. Tsirlin, M. Belesi, A. A. Leonov, U. K. Rößler, J. van den Brink, H. Rosner, The quantum nature of skyrmions and half-skyrmions in Cu_2OSeO_3. *Nat. Commun.* **5**, 5376 (2014).
31. A. Aqeel, N. Vlietstra, A. Roy, M. Mostovoy, B. J. van Wees, T. T. M. Palstra, Electrical detection of spiral spin structures in Pt|Cu_2OSeO_3 heterostructures. *Phys. Rev. B* **94**, 134418 (2016).
32. D. Coffey, T. M. Rice, F. C. Zhang, Erratum: Dzyaloshinskii-Moriya interaction in the cuprates [*Phys. Rev. B* 44, 10 112 (1991)]. *Phys. Rev. B* **46**, 5884 (1992).
33. J.-W. Bos, C. V. Colin, T. T. M. Palstra, Magnetoelectric coupling in the cubic ferrimagnet Cu_2OSeO_3. *Phys. Rev. B* **78**, 094416 (2008).
34. J. Romhányi, J. van den Brink, I. Rousochatzakis, Entangled tetrahedron ground state and excitations of the magnetoelectric skyrmion material Cu_2OSeO_3. *Phys. Rev. B* **90**, 140404 (R) (2014).
35. S. Seki, S. Ishiwata, Y. Tokura, Magnetoelectric nature of skyrmions in a chiral magnetic insulator Cu_2OSeO_3. *Phys. Rev. B* **86**, 060403(R) (2012).
36. M. Mochizuki, S. Seki, Dynamical magnetoelectric phenomena of multiferroic skyrmions. *J. Phys. Condens. Matter* **27**, 503001 (2015).
37. E. Ruff, P. Lunkenheimer, A. Loidl, H. Berger, S. Krohns, Magnetoelectric effects in the skyrmion host material Cu_2OSeO_3. *Sci. Rep.* **5**, 15025 (2015).
38. A. O. Leonov, "Twisted, localized, and modulated states described in the phenomenological theory of chiral and nanoscale ferromagnets," thesis, Technical University of Dresden (2012).
39. F. Qian, H. Wilhelm, A. Aqeel, T. T. M. Palstra, A. J. E. Lefering, E. H. Brück, C. Pappas, Phase diagram and magnetic relaxation phenomena in Cu_2OSeO_3. *Phys. Rev. B* **94**, 064418 (2016).
40. I. Živković, D. Pajić, T. Ivek, H. Berger, Two-step transition in a magnetoelectric ferrimagnet Cu_2OSeO_3. *Phys. Rev. B* **85**, 224402 (2012).

Acknowledgments: The authors acknowledge fruitful discussions with A. Bogdanov. G. Blake and Y. Prots are acknowledged for orienting the single crystals. **Funding:** F.Q. acknowledges financial support from the China Scholarship Council. C.P. and L.J.B. acknowledge Nederlandse Organisatie voor Wetenschappelijk Onderzoek Groot grant no. LARMOR 721.012.102. C.P. and M.M. acknowledge Vrije FOM-programma "Skyrmionics." A.O.L. thanks Ulrike Nitzsche for technical assistance and acknowledges Japan Society for the Promotion of Science (JSPS) Core-to-Core Program, Advanced Research Networks, and JSPS Grant-in-Aid for Research Activity Start-up 17H06889. This research used resources at the High Flux Isotope Reactor, a U.S. Department of Energy Office of Science User Facility operated by the Oak Ridge National Laboratory. **Author contributions:** F.Q. performed the magnetization and susceptibility measurements with the help of A.J.E.L. and E.B. F.Q., L.J.B., and C.P. performed the neutron scattering experiments with the support of G.C. and L.M.D.-S. A.A. and T.T.M.P. provided the samples for the magnetization and susceptibility measurements. M.P.S. provided the samples for the neutron scattering measurements. A.O.L. and M.M. developed the two complementary theoretical approaches. The study was conceived by C.P. in collaboration with H.W. C.P. supervised the project. The manuscript was written by F.Q., L.J.B., H.W., C.P., M.M., and A.O.L. **Competing interests:** The authors declare that they have no competing interests. **Data and materials availability:** All data needed to evaluate the conclusions in the paper are present in the paper and/or the Supplementary Materials. Additional data related to this paper may be requested from C.P. (c.pappas@tudelft.nl).

Submitted 3 April 2018
Accepted 8 August 2018
Published 21 September 2018
10.1126/sciadv.aat7323

Citation: F. Qian, L. J. Bannenberg, H. Wilhelm, G. Chaboussant, L. M. Debeer-Schmitt, M. P. Schmidt, A. Aqeel, T. T. M. Palstra, E. Brück, A. J. E. Lefering, C. Pappas, M. Mostovoy, A. O. Leonov, New magnetic phase of the chiral skyrmion material Cu_2OSeO_3. *Sci. Adv.* **4**, eaat7323 (2018).